Supplementary Material

CONTENTS

Samples

The nickelate thin films investigated in this study were synthesized via a two-step process involving pulsed laser deposition of the perovskite precursor material $R_{1-x}Sr_xNiO_3$ with rare-earth elements R = La, Nd, followed by topochemical reduction into the infinite layer phase $R_{1-x}Sr_xNiO_3$. The thin films were grown on either LSAT (001) or STO (001) single crystal substrates. The substrates were pre–treated with acetone/isopropyl alcohol ultra–sonication. The $SrTiO_3$ substrates also require a high-temperature anneal at 900 °C for 30 minutes in an oxygen partial pressure of 2×10^{-6} Torr. The growth conditions for all samples are otherwise equivalent.

The nickelate films were deposited at 570 °C in an oxygen partial pressure of 0.15 - 0.2 Torr. The resulting perovskite precursor films were then wrapped in aluminum foil and reacted with 0.15 g CaH_2 powder within a vacuum-sealed Pyrex glass tube (< 5 mtorr). The tube was heated to a temperature of 240 - 320 °C and annealed until a complete structural transition into the infinite layer phase was achieved. Further details on the fabrication process are described in the Supplementary Materials of Ref. [1], and the Extended figures of Ref. [2] for the $La_{0.8}Sr_{0.2}NiO_2$ and $Nd_{0.825}Sr_{0.175}NiO_2$ films, respectively.

The $La_{0.8}Sr_{0.2}NiO_2$ sample studied in this work is one of eight 2.5×5 mm pieces constituting the mosaic of samples measured by Fowlie et al [1]. The $La_{0.8}Sr_{0.2}NiO_2$ sample was was grown on $SrTiO_3$ substrate with a reduced phase thickness of 7.7 nm, and includes a 13.6 nm $SrTiO_3$ capping layer. Resistivity measurements of the sample were repeated right after the magneto–optical measurement were conducted, and reduction of Tc due to slow degradation with time was observed (see Fig. 1) compared to the state of the sample at the time of μSR measurements [1].

The $Nd_{0.825}Sr_{0.175}NiO_2$ samples were grown specifically for this study, and feature a reduced phase thickness of approximately 5 nm with a 1.5 nm $SrTiO_3$ capping layer. Resistivity of all samples is shown in Fig. 5 of the main text.

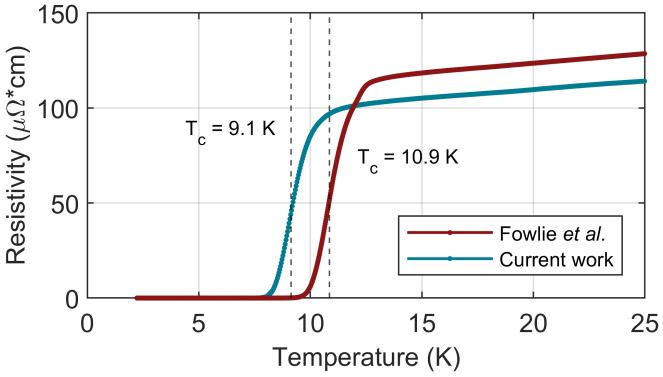

FIG. 1: **Resistivity of $La_{0.8}Sr_{0.2}NiO_2$.** Resistivity of LSNO-on-STO sample measured in the present study compared to the same measurement done at the time of publication of Ref. [1]. Superconducting transition temperatures T_c were determined as the mean of inflection point temperature and half–normal point temperature.

Zero-area-loop Sagnac interferometer

Design of fiber–optic zero loop area fiber Sagnac interferometer (ZALSI) [3] used in the present study is schematically illustrated on Fig. 2 . Continuous wave superluminescent diode (SLED) with 1550 nm center wavelength is used to emit light into polarization–maintaining (PANDA) fiber, which is split equally between slow and fast axis of the fiber using a polarizer oriented at 45^o degrees. Due to finite bandwidth of about 50 nm the SLED spectrum, two beams propagating along orthogonal axis of the fiber can be considered non-coherent after traveling for just 10 cm along the PM fiber with birefringence $\Delta n = 4 \times 10^{-4}$. Each light wave–pocket passes through the quarter–wave plate and is converted to right and left circularly polarized beams (which do no add up to a linearly polarized light since they are decoherent). Upon reflection from the sample, say, right–circularly polarized $\mathbf{E} = E_0 e^{-ikz}(\hat{x} + i\hat{y})$ light will acquire phase and amplitude change different from left–circularly polarized light *only if* time-reversal symmetry is broken in the material [4]. Upon reflection polarization of the light is fully converted to left–circularly polarized light $\mathbf{E}' = E_0 e^{ikz}(\hat{x} + i\hat{y})e^{-i\theta_K}$ which after passing quarter–wave plate goes into complimentary fast axis of the fiber. Similarly, light beam traveling along the fast–y axis to

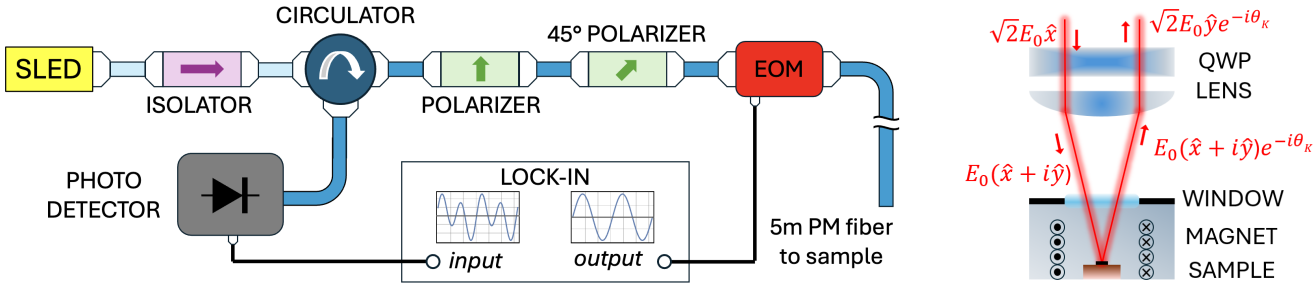

FIG. 2: **ZALSI.** Schematics of the zero-area-loop fiber-optic Sagnac interferometer. **Left panel**: fiber-optics components. Superluminescent diode (SLED) at 1550 nm with 50 nm bandwidth, single mode fiber (light blue), isolator, circulator, polarization–maintaing (PM) fiber (dark blue), polarizer along slow axis of the fiber and at 45 degrees between slow and fast axis, electro–optical modulator (EOM), 5 meter fiber patch, photodetector with 125 MHz bandwidth and AC coupled output, lock–in amplifier. In practice, circulator with fast–axis blocking is used to eliminate the need of in–fiber polarizer, and input port of EOM is aligned at 45^o with respect to fiber axis, which is schematically represented as stand–alone 45^o polarizer, which is likewise not present in our apparatus. **Right panel**: schematics of free–space components and cryogenic parts. Quarter–wave plate (QWP), lens with 50 mm focal length, fused silica window at top of the cryostat, coil magnet, sample glued to copper cold–finger.

the sample, propagates along the slow–x axis back from the sample. Once the beams reach the 45^o degree again, they have traveled the same optical length, hence they interfere, and interference pattern is sensitive to $2\theta_K$ phase shift between the beams.

Importantly, our apparatus is robust against any time–reversal preserving optical activities such linear birefringence or chirality, because these activities would only result in a mix of right and left circularly polarized (elliptically polarized) light after reflection, but would not change the interference pattern at the detector. Indeed, if, say some part of the light beam traveling along the slow axis of the fiber gets reflected back into the slow axis, by the time it reaches the detector it would have acquired such a phase $\varphi_{xx} = 2n_{\rm slow}L$, where $L \simeq 5$ m is the distance between the 45^o degree polarizer and the sample. Only the beams traveling along the time-reversal symmetric copies of each others path and acquiring phase $\varphi_{xy} = n_{\rm slow}L + n_{\rm fast}L$ will interfere as guaranteed by finite bandwidth of the source and a long 5 m fiber patch.

In order to measure phase shift $2\theta_K$ induced by magneto–optical Kerr effect, we use an electro–optical modulator (EOM) to modulate the phase of the light passing through the slow axis of the fiber (see Fig. 2). As a result, it can be shown using straightforward Jones analysis of polarization state of the light along the beam path, that for an arbitrary sample described by Jones matrix

$$J_{\rm sample} = \begin{pmatrix} R_+ & R_\mp \\ R_\pm & R_- \end{pmatrix} \tag{A.1}$$

power at the detector (up to an overall factor) is given by

$$P = |R|^2 + 2|R_+R_-|\cos 2\left[\theta_K - \phi_m \sin(\omega t + \delta)\right], \tag{A.2}$$

where first term $|R|^2 \equiv |R_+|^2 + |R_\pm|^2 + |R_\mp|^2 + |R_-|^2$ is the total power without modulation and interference, while the second term comes from interfering two counter–propagating beams. Phase shift $\delta = (\omega - \omega_p)\frac{\tau}{2}$ is the phase acquired from traveling from EOM to the sample and back. We fix modulation frequency to a proper value $\omega_p = \frac{\pi}{\tau} \simeq 10$ MHz determined by the time τ it takes the light to make the round trip. In doing so we minimize contribution from the residual–amplitude modulation, which is ignored in the formulas above and below. Producing Fourier decomposition of signal (A.2) we split the signal into three main components:

$$P'_0 = \frac{|R|^2}{2|R_+R_-|} + J_0(2\phi_m), \tag{A.3}$$

$$P'_\omega = 2\sin(2\theta_K)J_1(2\phi_m)\sin(\omega t + \delta), \tag{A.4}$$

$$P'_{2\omega} = 2\cos(2\theta_K)J_2(2\phi_m)\cos(2\omega t + 2\delta). \tag{A.5}$$

where J_1 and J_2 are Bessel functions and we re-scaled power

$$P' = \frac{P}{2|R_+R_-|}$$

for brevity. From here we see that first harmonic P_ω is only present when $\theta_K \neq 0$, and Kerr angle can be calculated as

$$\theta_K = \frac{1}{2}\tan^{-1}\left[\frac{J_2(2\phi_m)V_\omega^{\rm RMS}}{J_1(2\phi_m)V_{2\omega}^{\rm RMS}}\right], \tag{A.6}$$

which is independent of optical power or sample reflectivity. Here $V_\omega^{\rm RMS} \propto P_\omega$ is the voltage reading on the lock–in amplifier. Finally, to maximize signal–to–noise ratio we set modulation amplitude value ϕ_m and first lock–in phase δ such that first harmonic is maximized when measured from a magnetic material.

Our apparatus has proven itself an extremely sensitive magneto–optical measurement technique, which agrees

with other Kerr angle probes when tested on a strongly magnetic materials, and at the same time is able to detect much smaller signals unreachable via different MOKE experimental tests, as it is evident from the recent study of charge order in CsV_3Sb_5 [5, 6]. Due to remarkably high shot–noise–limited sensitivity of 100 nrad/$\sqrt{\text{Hz}}$ zero loop area Sagnac interferometer is even able to observe a time-reversal breaking superconducting order parameter in heavy–fermion materials Sr_2RuO_4 [7], UPt_3 [8] and UTe_2 [9, 10], as well as many other phenomena.

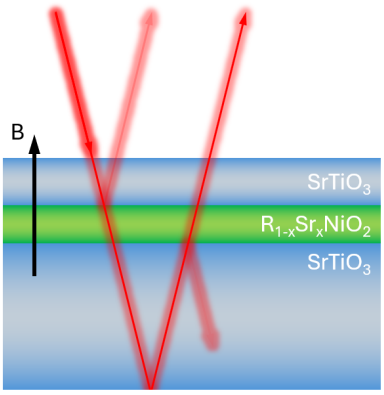

FIG. 3: **Schematic propagation of light.** Reflected light is a combination of beams reflected different surfaces.

Relationship between MOKE and magnetization

Light beam experiences several reflections upon its optical path on each interface. However STO capping layer and substrate are transparent, while nickelate layer is mostly transparent. It has resistivity of $\rho \simeq 200$ μOhm*cm which correspond to skin–depth $\delta \simeq 50$ nm, much larger then sample's thickness of $d \simeq 5$ nm. Overall, returned light is mostly composed of the light reflected from the bottom surface of the substrate with small contribution from the metallic surface (see Fig.Fig. 3). As a result (in the absence of magnetic field) measured optical rotation consists mostly of combination of two Faraday angle acquired upon propagation in two different directions.

$$\theta_K^{\text{total}} \simeq \theta_F^{\swarrow} + \theta_F^{\nearrow}. \tag{A.7}$$

It is important to highlight that Faraday effect measured in transmission only can be present due to non–magnetic types of optical activities, such as birefringence or dichroism, however, a combination of two counter–propagating Faraday rotations has the same symmetry as a Kerr angle [4]. Situation is more complicated, however, in the presence of external magnetic field, since then the substrate contributes to the optical rotation as well.

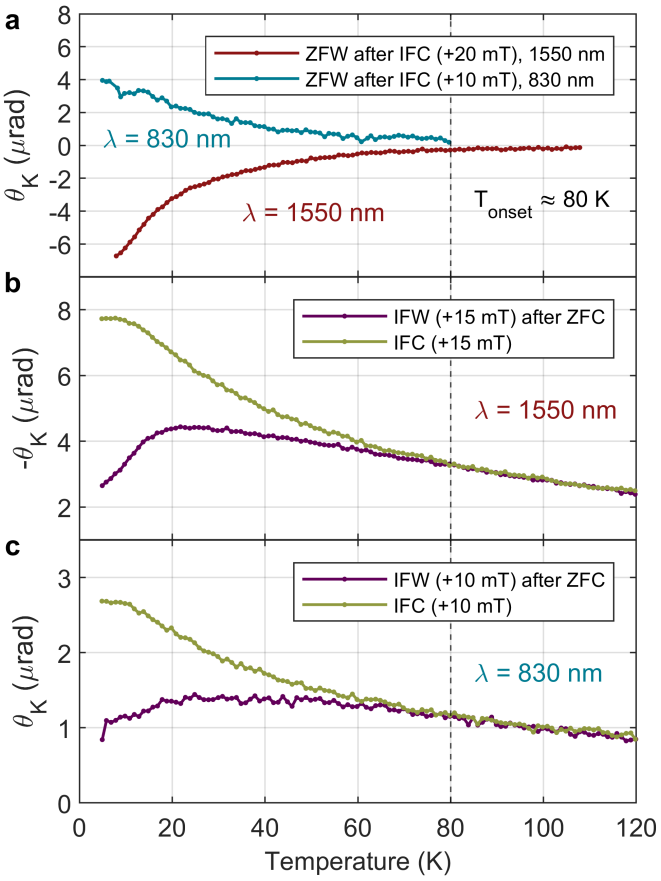

FIG. 4: **Wavelength dependence of MOKE.** Kerr signal in $La_{0.8}Sr_{0.2}NiO_2$ vs temperature measured with two different ZALSI interferometers operating at 1550 and 830 nm. **a** Zero-field warmup after training in positive field at two different wavelengths. **b** In-field warmup/cooldown measured at 1550 nm. **c** In-field warmup/cooldown measured at 830 nm.

As follows directly from Fresnel equations, Kerr and Faraday rotations are given by [11]

$$\theta_K = \text{Re}\left\{\frac{\sigma_{xy}}{\sigma_{xx}\left[1+4\pi i\sigma_{xx}/\omega\right]^{1/2}}\right\}, \tag{A.8}$$

$$\theta_F = \frac{2\pi d}{c}\,\text{Re}\left\{\frac{\sigma_{xy}}{\left[1+4\pi i\sigma_{xx}/\omega\right]^{1/2}}\right\}, \tag{A.9}$$

where d is the thickness of the material. The meaning behind this equation is simple: when electromagnetic wave propagates inside the media, it constantly "shakes" electrons, which in turn re–emitted the light as radiation, however in the presence of magnetic moment, electron's orbital motion is curved (described by finite $\sigma_{xy}(\omega)$), which finally leads to rotation of polarization. Such optical activity is known as gyrotropy and is characteristic to many magnetic materials [12]. What is not generally simple is a relation between Hall conductivity $\sigma_{xy}(\omega)$

and magnetization M_z at optical frequencies, since it's determined by the exact structure of all the allowed optical transitions. In general, Hall conductivity $\sigma_{xy}(\omega)$ typically changes sign as a function of light energy (wavelength).

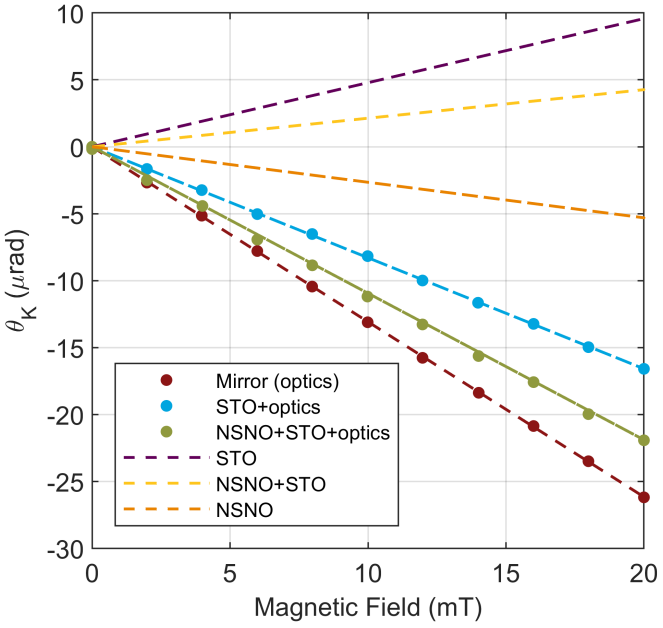

FIG. 5: **MOKE vs Magnetic Field.** Kerr signal as a function of applied magnetic field at $T = 150$ K. Circle points represent measured data and dashed lines correspond to linear fit.

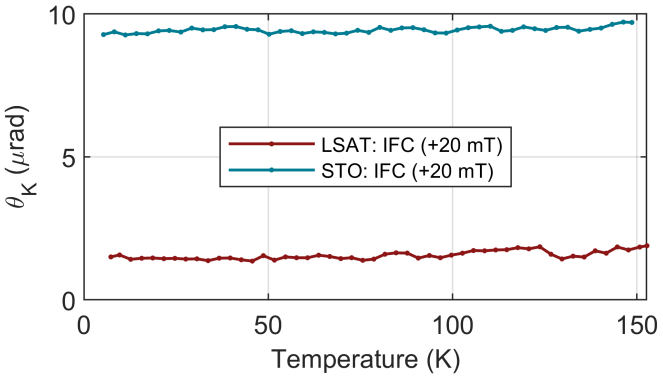

FIG. 6: **MOKE in STO and LSAT.** Paramagnetic–like Kerr signal in $SrTiO_3$ and $(LaAlO_3)_{0.3}(Sr_2TaAlO_6)_{0.7}$ substrates measured during cooldown in $B = +20$ mT magnetic field. Contribution from optics was subtracted.

In–field MOKE measurements

All measurements performed in the presence of magnetic field suffer from background signal caused by Faraday effect in optical elements along light's path: quarter–wave plate, lens, and cryostat window all contribute to measured MOKE value. This additional wavelength–dependent linear–in–field part of the signal can be estimated based on Verdet constant of the material, thickness of optical elements and magnetic field they experience. However, in practice magnetic field varies with distance from the cryostat, which results in noticeable change in measured signal even when lens is moved by 1 mm, so it is easier to measure contribution from optics by placing a mirror (non–magnetic reflecting material) next to the sample and measuring signal from it.

Results of such calibration measurement performed on NSNO–on–STS sample, STO substrate, and mirror are shown on Fig. 5 . Magnetic field sweeps were performed at $T = 150$ K, where no history–depended spin–glass dynamics is expected to be present. Kerr rotation measured off of the mirror, comes fully from the Faraday rotation happening in the optical elements, and is as expected negative in positive field, due to negative Verdet constant of fused silica glass $V_{\text{glass}} \simeq 2.5$ rad·T^{-1}·m^{-1} at 1550 nm. Measurement of $SrTiO_3$ substrate result in a combination of positive paramagnetic–like contribution from the substrate and negative signal from the optics, subtracting the value recorded off of mirror, we can isolate Kerr rotation produced by $SrTiO_3$ substrate. Finally, to separate signal from the nickelate we look at the difference between Kerr signal detected from the sample and from the substrate. Due to many factors, such as non–uniformity of magnetic field around the optical components, affect of the annealing procedure that the samples goes through on the substrate, we do not expect described subtraction procedure to result in perfect isolation of the signal coming form the sample. However, as seen from Fig. 6 signal from substrate is constant in temperature, hence contribution from the substrate only affect overall constant background, which is not important for the SG state analysis.

Furthermore, we repeat substrate measurement at fixed applied magnetic field of +20 mT and sweep the temperature to obtain data presented on Fig. 6 . We observe almost no temperature dependence of STO–induced Kerr signal, which lets us conclude that observed glassy phase (Fig. 1 of the main text) is coming fully from the sample.

Lastly, let us emphasize that unlike in–field measurement, running experiment in the at $B = 0$ mT has no such drawbacks, hence there is no need to perform a background subtraction for the zero–field warmup datasets.

Examination of NiO_x inclusions

To address the question of the effect of NiO_x inclusions on our measurements, we provide atomic force microscopy data in Fig. 7 . In Ref. [13], NiO_x particles were found on the interface between infinite–layer nickelate and the

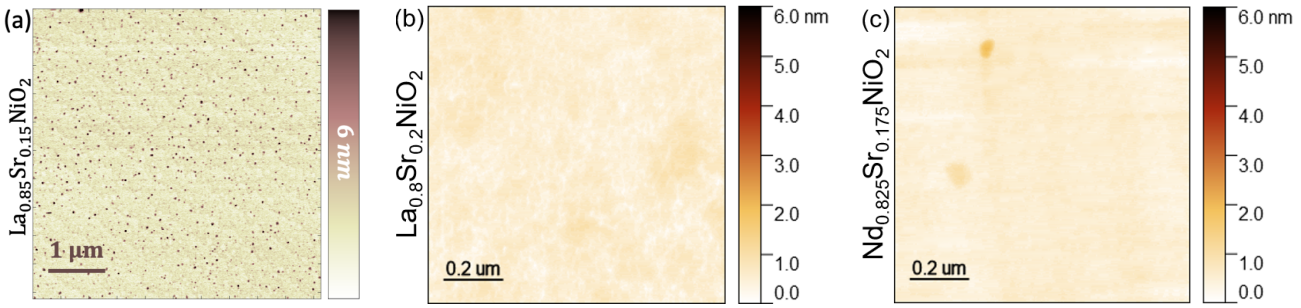

FIG. 7: AFM scans of LSNO/STO and NSNO/STO. (a) Pasted from Ref. [13] (b,c) LSNO/STO and NSNO/STO samples that were measured in our paper. The AFM images of infinite layer nickelates grown on $SrTiO_3$ substrate show a sufficiently low surface particle density to cause any potential background from NiO_x inclusions to be minimal. The planar density of surface particles is significantly lower than that reported in ref X., given similar scan sizes in AFM images.

capping STO layer, and the observed ferromagnetic signal was attributed to these particles. Specifically, the authors of Ref. [13] used STEM-EELS data to identify the particles and, using atomic force microscopy, found a typical density of 37.5 particles per μm^2. Each particle was clearly visible in the AFM as a 6 nm tall protrusion. We present AFM scans of our samples which show that the top surface of our LSNO/STO and NSNO/STO samples have root-mean-square roughness of less then 1 nm. This evidence demonstrates that current generation of thin–film infinite layer nickelate samples has negligible concentration of NiO_x inclusions.

[1] J. Fowlie, M. Hadjimichael, M. M. Martins, D. Li, M. Osada, B. Y. Wang, K. Lee, Y. Lee, Z. Salman, T. Prokscha, *et al.*, Nature Physics **18**, 1043 (2022).

[2] K. Lee, B. Y. Wang, M. Osada, B. H. Goodge, T. C. Wang, Y. Lee, S. Harvey, W. J. Kim, Y. Yu, C. Murthy, S. Raghu, L. F. Kourkoutis, and H. Y. Hwang, Nature **619**, 288 (2023).

[3] J. Xia, P. T. Beyersdorf, M. M. Fejer, and A. Kapitulnik, Applied Physics Letters **89**, 062508 (2006).

[4] B. I. Halperin, in *The Physics and Chemistry of Oxide Superconductors*, edited by Y. Iye and H. Yasuoka (Springer Berlin Heidelberg, Berlin, Heidelberg, 1992) pp. 439–450.

[5] D. R. Saykin, C. Farhang, E. D. Kountz, D. Chen, B. R. Ortiz, C. Shekhar, C. Felser, S. D. Wilson, R. Thomale, J. Xia, and A. Kapitulnik, Phys. Rev. Lett. **131**, 016901 (2023).

[6] C. Farhang, J. Wang, B. R. Ortiz, S. D. Wilson, and J. Xia, Nature Communications **14**, 5326 (2023).

[7] J. Xia, Y. Maeno, P. T. Beyersdorf, M. M. Fejer, and A. Kapitulnik, Phys. Rev. Lett. **97**, 167002 (2006).

[8] E. R. Schemm, W. J. Gannon, C. M. Wishne, W. P. Halperin, and A. Kapitulnik, Science **345**, 190 (2014).

[9] I. M. Hayes, D. S. Wei, T. Metz, J. Zhang, Y. S. Eo, S. Ran, S. R. Saha, J. Collini, N. P. Butch, D. F. Agterberg, A. Kapitulnik, and J. Paglione, Science **373**, 797 (2021).

[10] D. S. Wei, D. Saykin, O. Y. Miller, S. Ran, S. R. Saha, D. F. Agterberg, J. Schmalian, N. P. Butch, J. Paglione, and A. Kapitulnik, Phys. Rev. B **105**, 024521 (2022).

[11] P. M. Oppeneer, *Theory of the magneto-optical Kerr effect in ferromagnetic compounds*, Ph.D. thesis (1999).

[12] L. D. Landau, J. S. Bell, M. Kearsley, L. Pitaevskii, E. Lifshitz, and J. Sykes, *Electrodynamics of continuous media*, Vol. 8 (elsevier, 2013).

[13] R. A. Shi, B. Y. Wang, Y. Iguchi, M. Osada, K. Lee, B. H. Goodge, L. F. Kourkoutis, H. Y. Hwang, and K. A. Moler, Physical Review Materials **8**, 024802 (2024).